Supplementary Information (SI) for Journal of Materials Chemistry A.

Supporting Information

Self-evolution Induced Cu_xO/Fe_3O_4 Heterogeneous Interfaces Enabling Rapid Nitrate Reduction to Ammonia

Yingjie Xia[1], Xin Li[1], Yansen Qu[1], Yi Zhou[1], Ziyang Weng[1], Shengming Jin[1], Jun Wang[1], Xinghua Chang[1,2,*]

1. School of Minerals Processing and Bioengineering, Central South University, Changsha 410083, China.

2. Key Laboratory for Mineral Materials and Application of Hunan Province, Central South University, Changsha 410083, China

E-mail: changxinghua@csu.edu.cn

1 Experimental Section

Reagents and chemicals

Sodium nitrate ($NaNO_3$, analytical grade) was purchased from Chengdu Chron Chemical Co., Ltd. Anhydrous sodium sulfate (Na_2SO_4, analytical grade), copper(II) nitrate trihydrate ($Cu(NO_3)_2$ $3H_2O$, analytical grade), and iron(III) nitrate nonahydrate ($Fe(NO_3)_3$ $9H_2O$) were obtained from Shanghai Aladdin Biochemical Technology Co., Ltd. 1,3,5-Benzenetricarboxylic acid (H_3BTC, 98%), N,N-dimethylformamide (DMF, 99.8%), and polyvinylpyrrolidone (PVP, K30) were purchased from Shanghai Macklin Biochemical Co., Ltd. High-purity hydrogen (H_2, 99.999%) and argon (Ar, 99.999%) were supplied by Changsha Saizhong Special Gas Co., Ltd. Nafion solution (5 wt%) and carbon cloth were sourced from DuPont, USA.

Preparation of Cu@NC, Cu_xFe@NC, and Fe@NC catalysts and working electrodes

Synthesis of Cu@NC, Cu_xFe@NC, and Fe@NC

A solution (Solution A) was prepared by dissolving $Cu(NO_3)_2$ $3H_2O$ and $Fe(NO_3)_3$ $9H_2O$ in different molar ratios (totaling 4.8 mmol) in 10 mL of N,N-dimethylformamide (DMF). Separately, another solution (Solution B) was prepared by dissolving 4.8 mmol of 1,3,5-benzenetricarboxylic acid (H_3BTC) and 0.215 g of polyvinylpyrrolidone (PVP) in 10 mL of DMF. Solution B was then added into Solution A, thoroughly mixed, and transferred to a stainless-steel autoclave lined with polytetrafluoroethylene (PTFE). The mixture was subjected to solvothermal treatment at 160°C for 1.5 hours. The resulting precipitate was collected via centrifugation, washed three times with anhydrous ethanol, and dried at 60°C for 12 hours, yielding a blue or reddish-brown powder—Cu_xFe-BTC precursors with different Cu/Fe ratios. The obtained Cu_xFe-BTC precursor was subsequently carbonized in a mixed H_2: Ar (10:90) atmosphere by heating at a rate of 10°C/min to 800°C, followed by a 2-hour dwell time. After cooling, the final Cu_xFe@NC catalyst material was obtained.[1,2]

Preparation of the working electrode

A total of 20 mg of the synthesized catalyst was dispersed in a 1.2 mL mixture of ethanol and water (ethanol: water = 2:1) along with 100 μL of Nafion solution (5 wt%). The solution was then ultrasonicated for 20 minutes to obtain a homogeneous catalyst ink. Subsequently, the catalyst ink was drop-cast onto a 2 × 2 cm^2 carbon cloth and allowed to dry at room temperature, resulting in the preparation of the working electrode.

Characterizations

Physical characterization of precursors and catalyst materials

The structure and morphology of the catalyst and its precursor were characterized using various analytical techniques. Scanning electron microscopy (SEM) (MIRA 3, TESCAN, Czechia) and transmission electron microscopy (TEM) equipped with an energy-dispersive X-ray spectrometer (FEI Titan G2 60-300, Super EDX) were used for imaging and elemental analysis. X-ray diffraction (XRD) with a Cu Kα source (TD-3500, Dandong Tongda, $\lambda = 1.5406$ Å) was employed to analyze the crystal structure within a scanning range of 5–80°. X-ray photoelectron spectroscopy (XPS) (Thermo Scientific K-Alpha) with an Al Kα excitation source (hv = 1486.6 eV) was utilized to determine the elemental composition and chemical states. Additionally, Fourier transform infrared spectroscopy (FTIR) (Nicolet iS50, Thermo Fisher, USA) was conducted to further investigate the chemical structure of the catalyst and precursor.

Electrochemical performance measurement

The electrochemical performance of the catalyst was evaluated using a three-electrode system consisting of a working electrode, a platinum counter electrode, and a saturated KCl Ag/AgCl reference electrode. The electrocatalytic nitrate reduction reaction was monitored using CHI 760 E and Gamry Interface 1010 (Gamry Instruments) electrochemical workstations, where LSV, CV, and EIS measurements were conducted. To investigate the dynamic surface changes of the catalyst and identify intermediate species during the reaction, in-situ Raman spectroscopy was performed using a Micro-Raman 126 spectrometer (InVia Qontor, Renishaw), while Fourier transform infrared spectroscopy (FTIR, Nicolet iS 50, Thermo Fisher, USA) was employed for further analysis. The concentrations of nitrate (NO_3^-), nitrite (NO_2^-), and ammonium (NH_4^+) were quantified using a UV-Vis spectrophotometer (Unico 2800, Thermo Fisher, USA). Additionally, a rotating disk electrode (RDE, AFMSRC, Pine, USA) was used to investigate the electrochemical nitrate reduction reaction at different rotation speeds, allowing for the determination of the number of electron transfers during the process.

Rotating Disk Electrode (RDE) calculation and fitting methodology

The working electrode was prepared by drop-casting the catalyst ink onto the glassy carbon RDE surface.[3,4] Prior to testing, the electrolyte solution was purged with high-purity nitrogen for 30 minutes to eliminate dissolved oxygen. Linear sweep voltammetry (LSV) measurements were conducted at various rotation speeds, and the corresponding current responses were recorded. To analyze mass transfer effects and determine the electron transfer number, the Koutecky-Levich (K-L) equation was applied:

$$\frac{1}{j} = \frac{1}{j_k} + \frac{1}{j_L}$$

where: j is the measured current density (mA cm^{-2}), j_k is the kinetic current density (mA cm^{-2}), j_L is the diffusion-limited current density (mA cm^{-2}), given by: $j_L = B\omega^{1/2}$.
where B is the Levich constant:

$$B = 0.62nFCD^{2/3}\upsilon^{-1/6}$$

where, n represents the number of electrons transferred, F is the Faraday constant (96485 C/mol), C denotes the nitrate concentration (mol/mL), D is the diffusion coefficient of NO_3^- in solution (~1.9×10^{-5} cm^2/s), υ is the kinematic viscosity of the electrolyte (~0.01 cm^2/s), and ω represents the electrode rotation speed (rpm).
At different potentials, a linear fitting curve of 1/j is plotted. The slope of the linear fit corresponds to the B value, which is used to calculate the number of electrons transferred (n).

$$n = \frac{B}{0.62FCD^{2/3}\upsilon^{-1/6}}$$

The electron transfer number is determined at various potentials, and its variation trend is analyzed to gain insights into the mechanism of the eNO_3RR process.

DFT calculations

We used the DFT as implemented in the Vienna Ab initio simulation package (VASP) in all calculations. The exchange-correlation potential is described by using the generalized gradient approximation of Perdew-Burke-Ernzerhof (GGA-PBE). The projector augmented-wave (PAW) method is employed to treat interactions between ion cores and valence electrons. The plane-wave cutoff energy was fixed to 450 eV. Given structural models were relaxed until the Hellmann–Feynman forces smaller than -0.02 eV/Å and the change in energy smaller than 10-5 eV was attained. Grimme's DFT-D3 methodology was used to describe the dispersion interactions among all the atoms in adsorption models.
The Gibbs free energy change is defined as:

$$\Delta G = \Delta E + \Delta ZPE - T\Delta S$$

where ΔE is the electronic energy calculated with VASP, ΔZPE and ΔS are the zero-point energy difference and the entropy change between the products and reactants, respectively, and T is the temperature (298.15 K).

2 Supplementary Figures

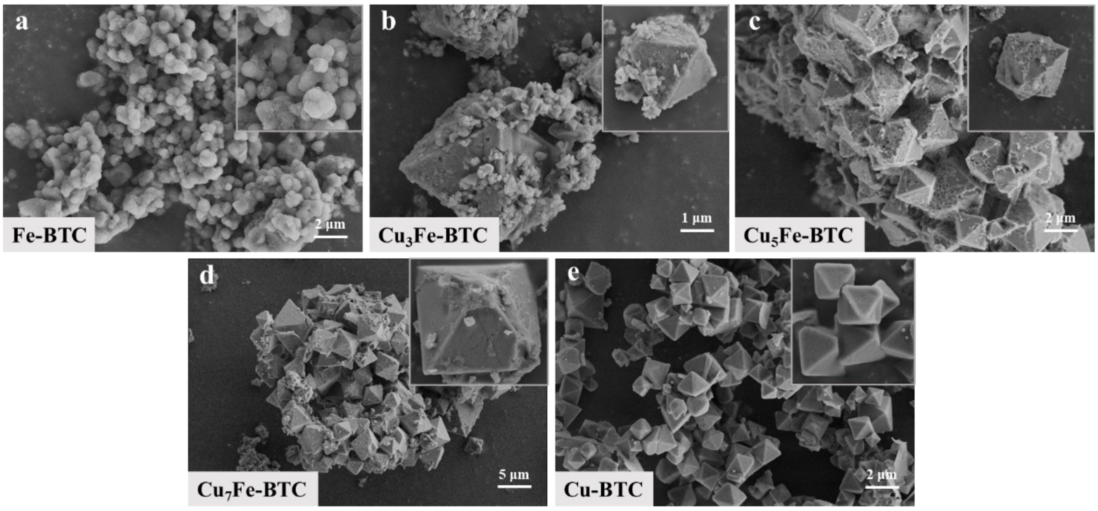

Figure. S1. (a–e) SEM images of Fe-BTC, Cu$_3$Fe-BTC, Cu$_5$Fe-BTC, Cu$_7$Fe-BTC, and Cu-BTC, respectively.

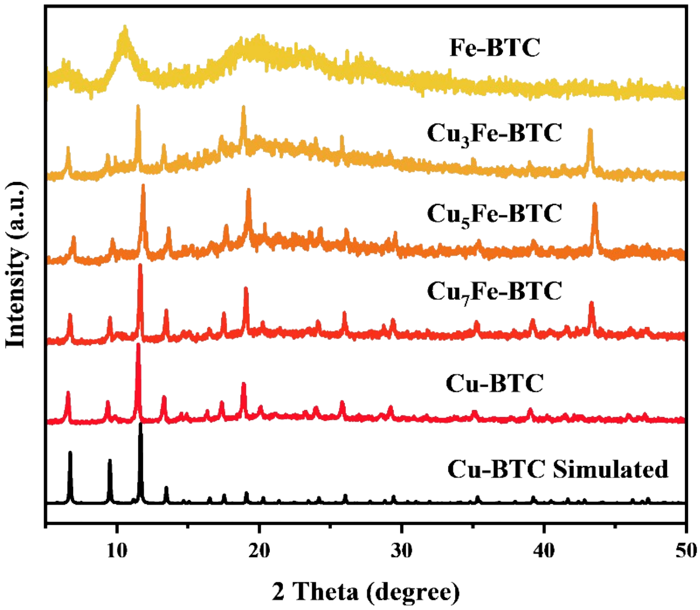

Figure. S2. XRD patterns of Cu$_x$Fe-BTC, Cu-BTC, and Fe-BTC.

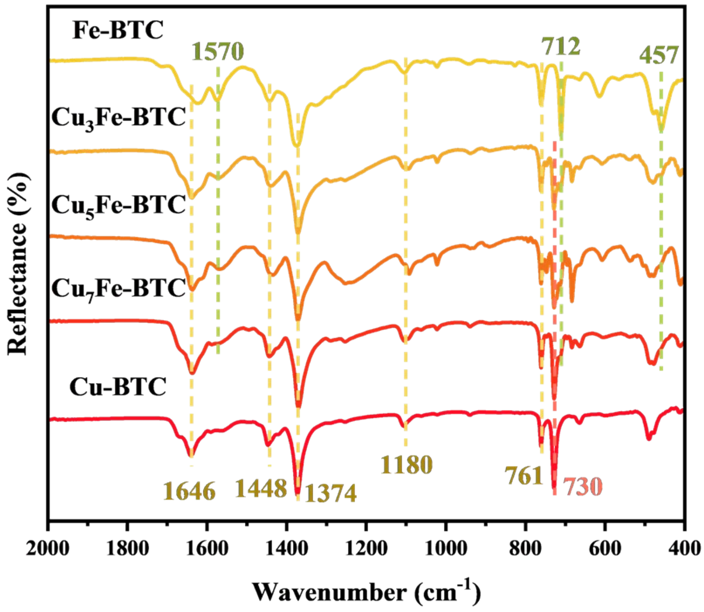

Figure. S3. FTIR spectra of Cu_xFe-BTC, Cu-BTC, and Fe-BTC.

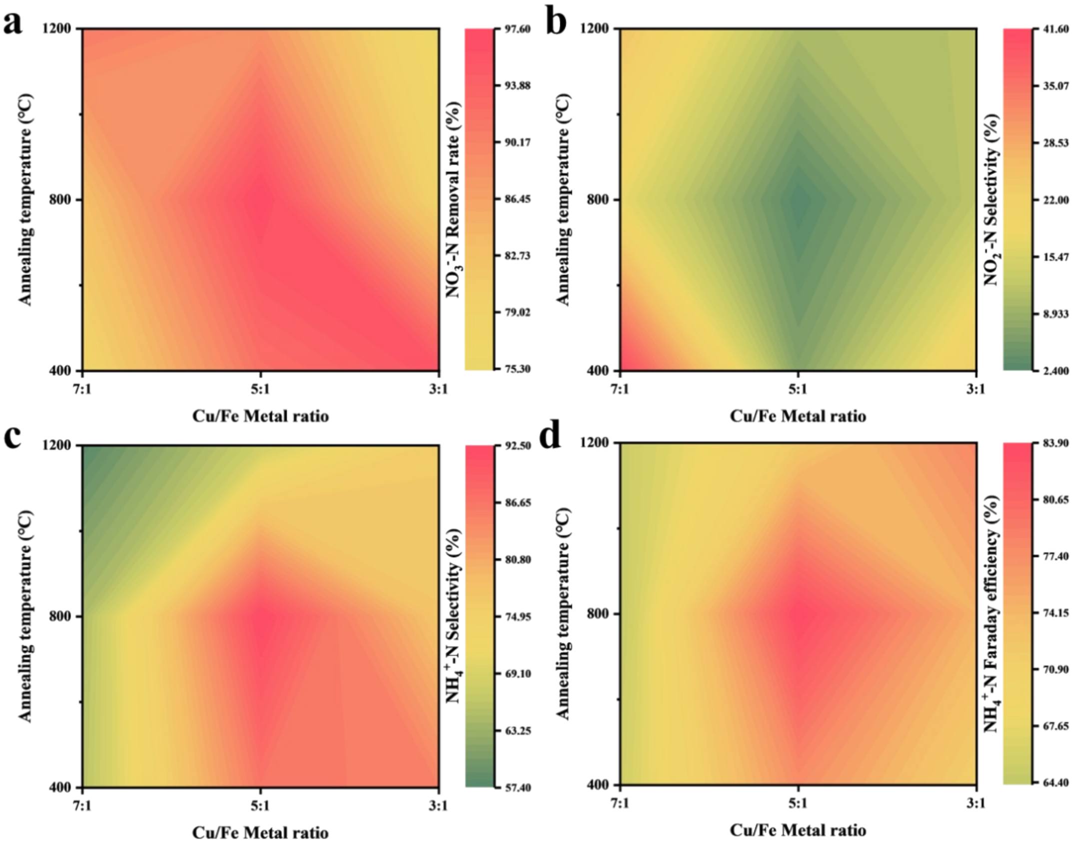

Figure. S4. (a–d) NO_3^--N removal rate, NO_2^--N selectivity, NH_4^+-N selectivity, and Faradaic efficiency at varying temperatures and Cu/Fe ratios.

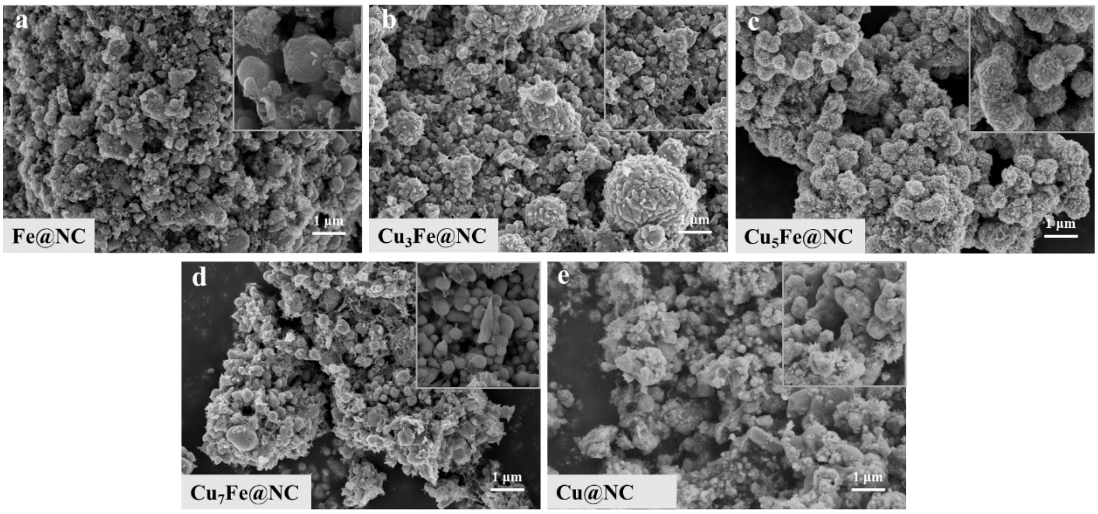

Figure. S5. (a–e) SEM images of Fe@NC, Cu_3Fe@NC, Cu_5Fe@NC, Cu_7Fe@NC, and Cu@NC.

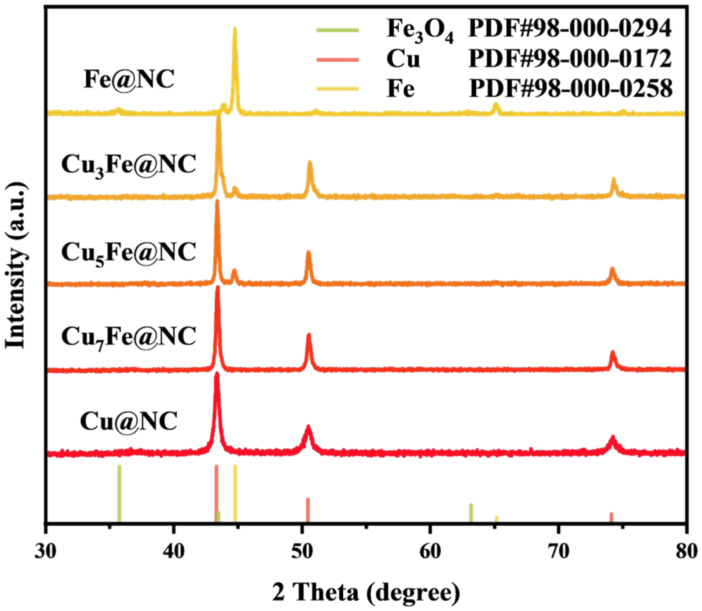

Figure. S6. XRD patterns of Cu_xFe@NC, Cu@NC, and Fe@NC.

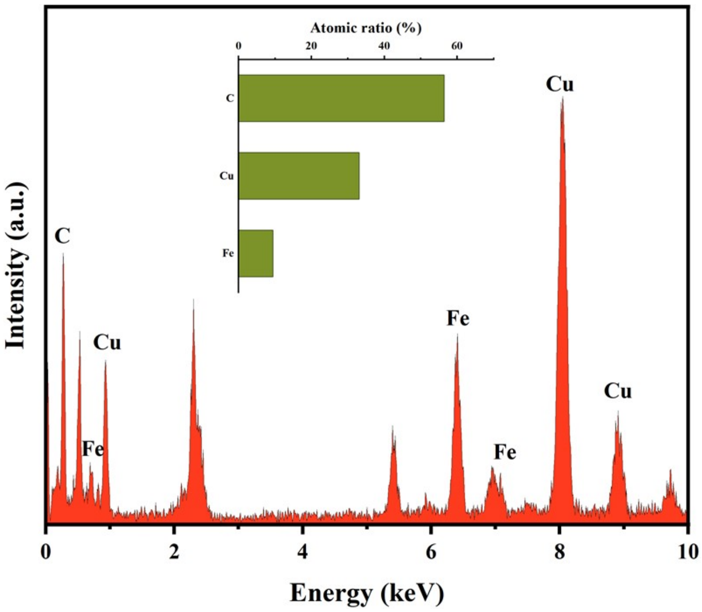

Figure. S7. EDS spectra of Cu_5Fe@NC.

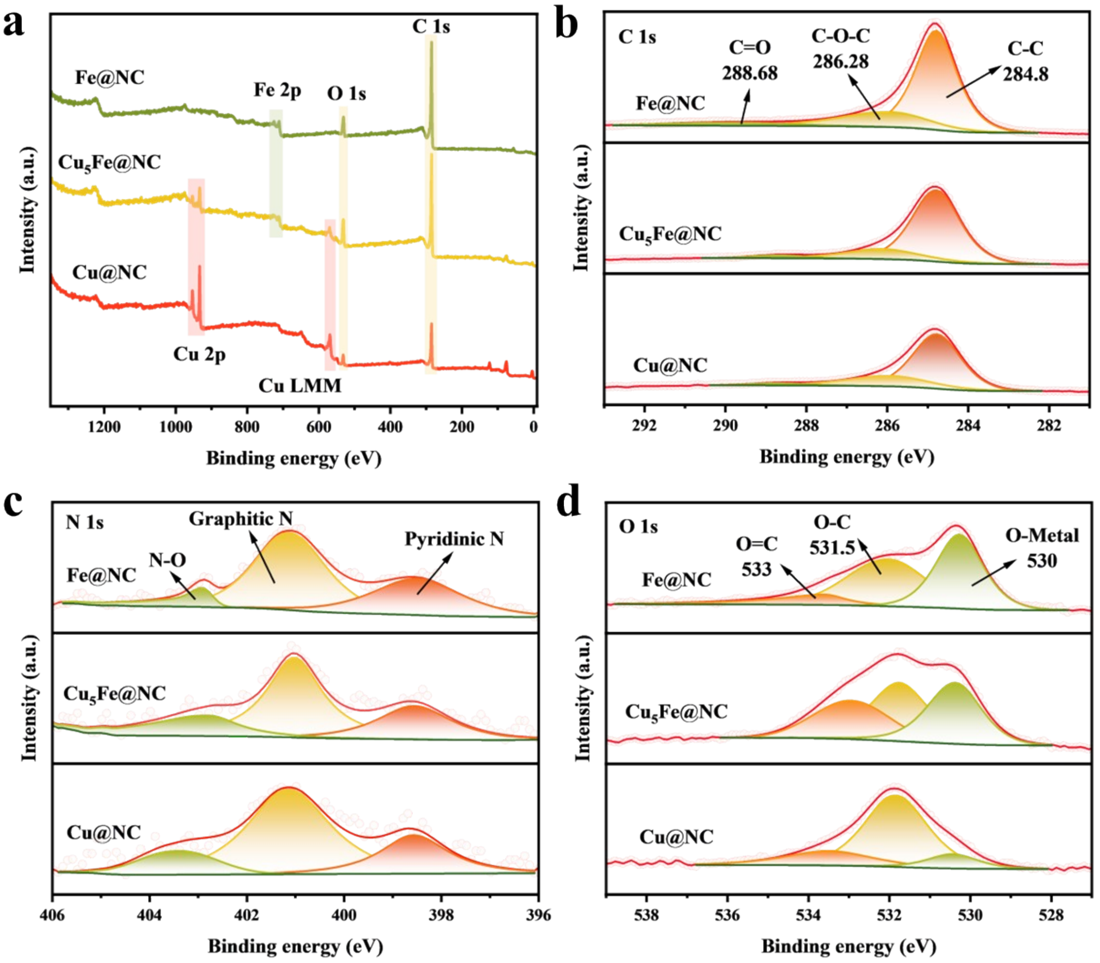

Figure. S8. a, b, c and **d** XPS survey spectra, along with high-resolution C 1s, N 1s and O 1s XPS spectra, of Cu@NC, Cu_5Fe@NC, and Fe@NC.

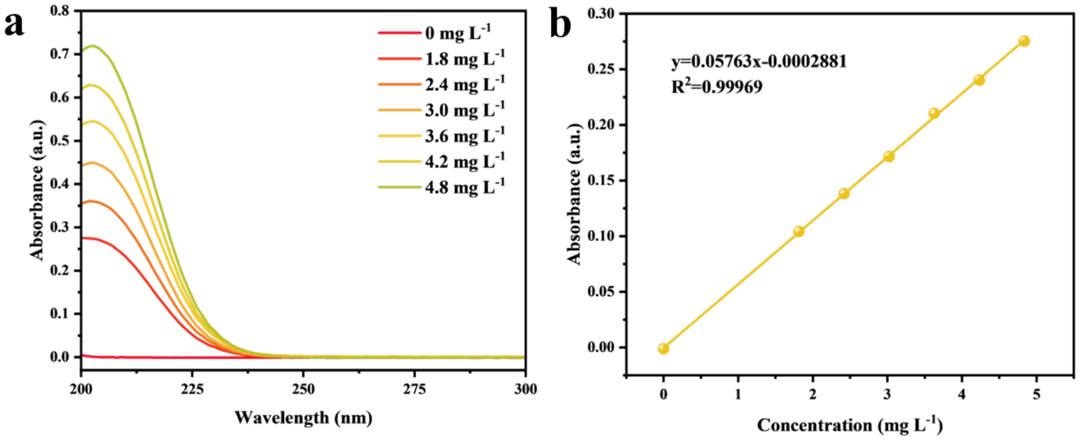

Figure. S9. **a** and **b** The UV-Vis absorption spectra of NO_3^--N, measured using the colorimetric method, along with the corresponding standard calibration curve.

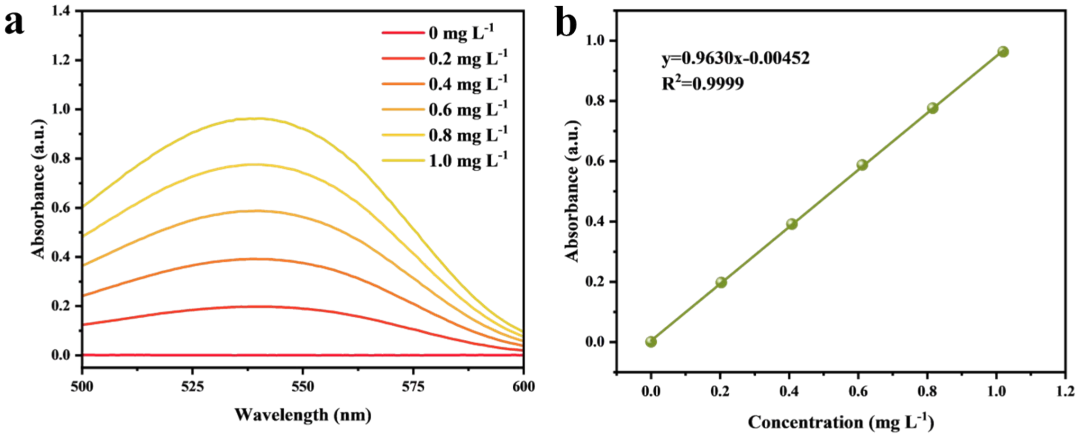

Figure. S10. **a** and **b** The UV-Vis absorption spectra of NO_2^--N, measured using the colorimetric method, along with the corresponding standard calibration curve.

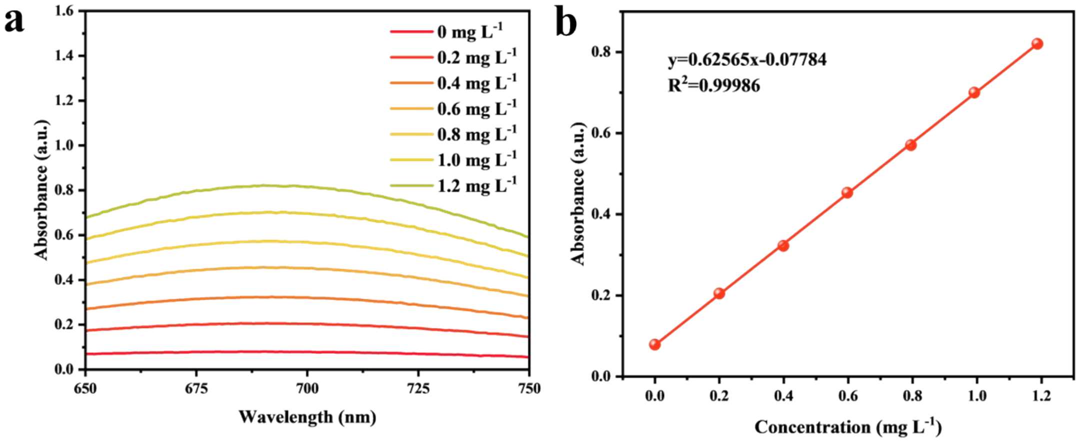

Figure. S11. **a** and **b** The UV-Vis absorption spectra of NH_4^+-N, measured using the colorimetric method, along with the corresponding standard calibration curve.

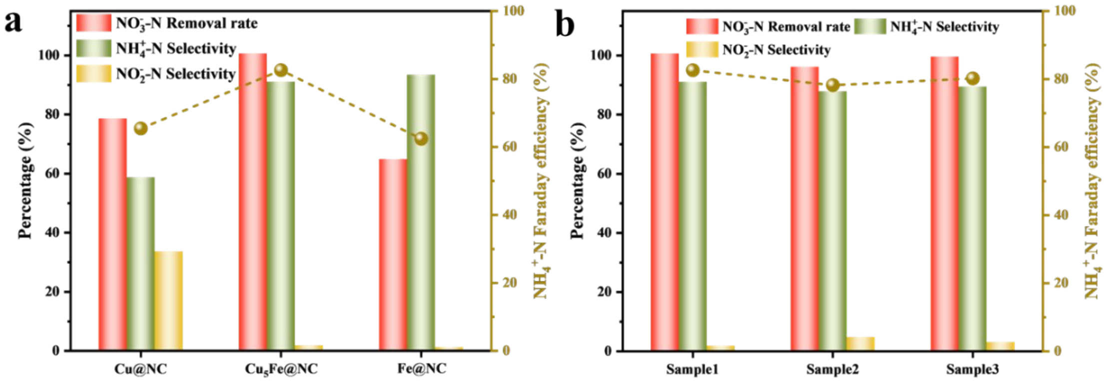

Figure. S12. a Electrocatalytic performance of Cu@NC, Cu_5Fe@NC, and Fe@NC in 0.01 M $NaNO_3$ electrolyte. **b** Batch-to-batch catalytic performance of Cu_5Fe@NC under identical conditions.

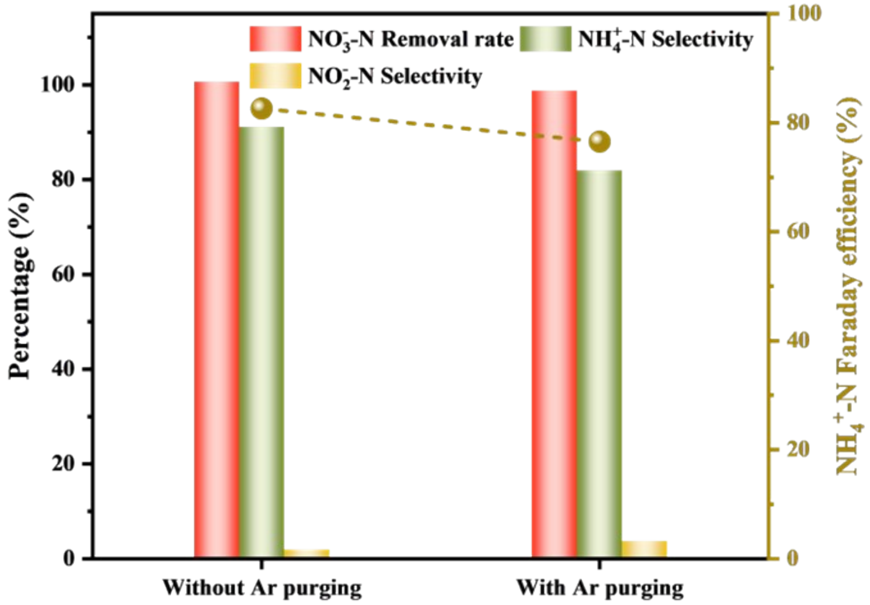

Figure. S13. Electrochemical performance of Cu_5Fe@NC with and without Ar purging.

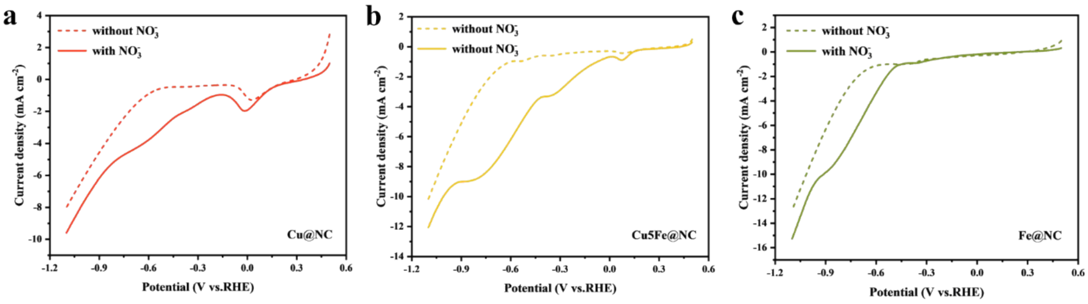

Figure. S14. a, b and **c** LSV curves of Cu@NC, Cu_5Fe@NC, and Fe@NC recorded at a sweep rate of 10 mV s^{-1} in both the presence and absence of nitrate.

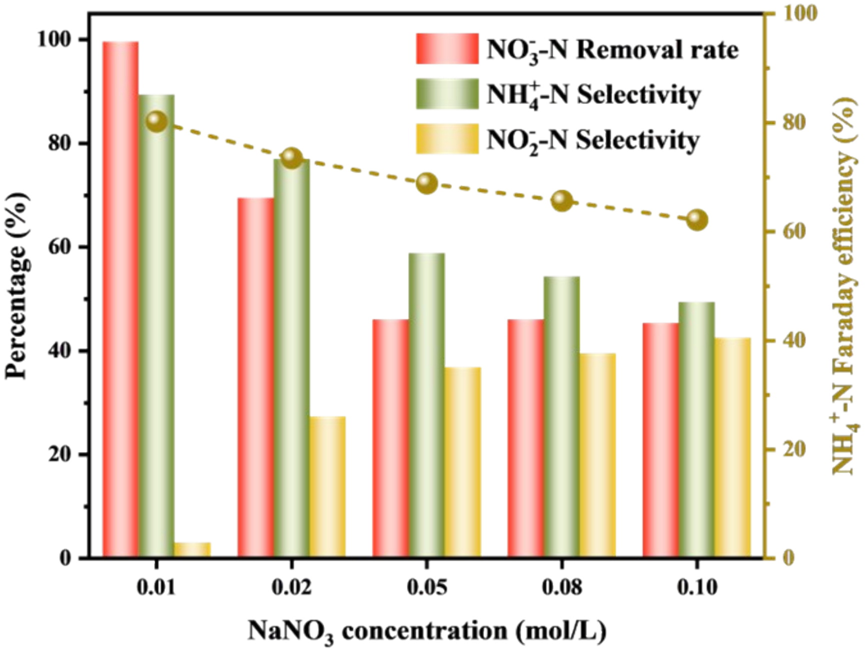

Figure. S15. Electrocatalytic performance of Cu_5Fe@NC under different nitrate concentrations.

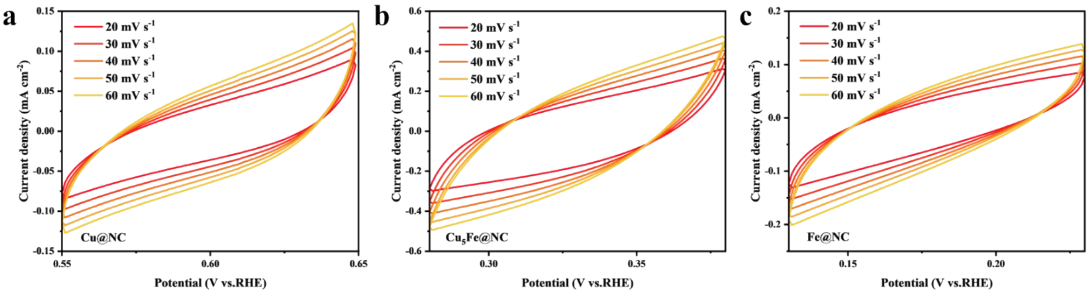

Figure. S16. a, b and **c** CV curves of Cu@NC, Cu_5Fe@NC, and Fe@NC recorded at scan rates ranging from 20 to 60 mV s^{-1}.

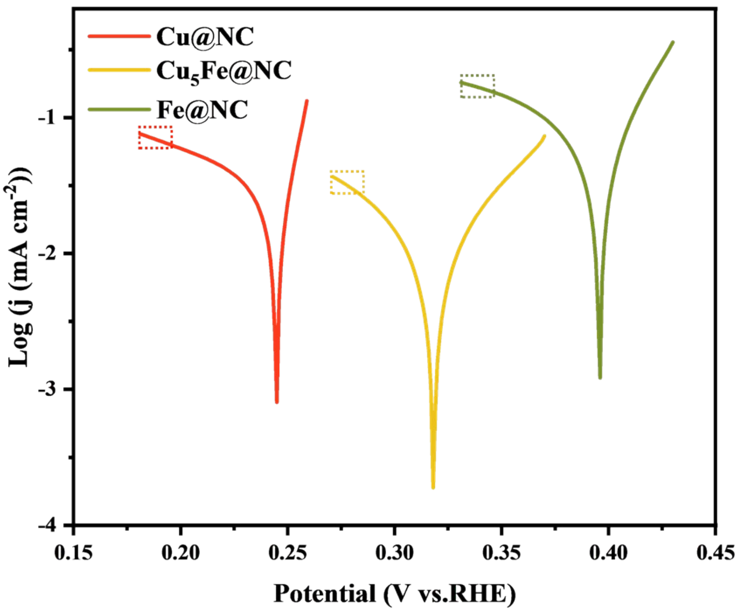

Figure. S17. Tafel plots of Cu@NC, Cu_5Fe@NC, and Fe@NC.

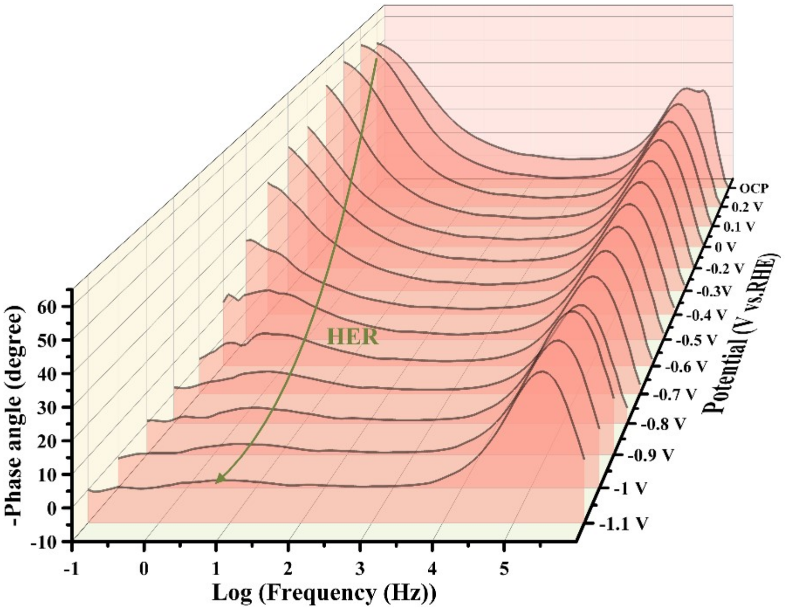

Figure. S18. Bode plots of Cu_5Fe@NC at various potentials in a nitrate-free system.

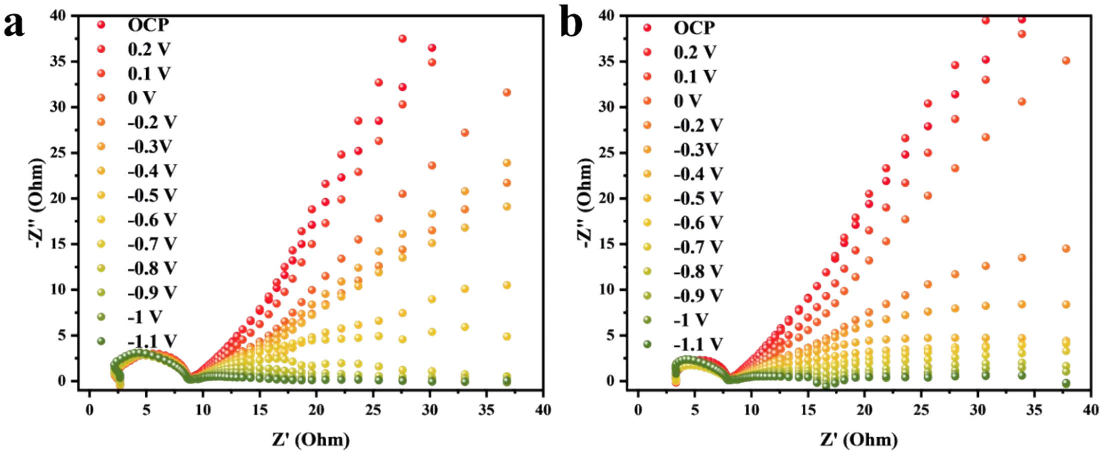

Figure. S19. a and **b** Nyquist plots of Cu$_5$Fe@NC at different potentials in both nitrate-containing and nitrate-free systems.

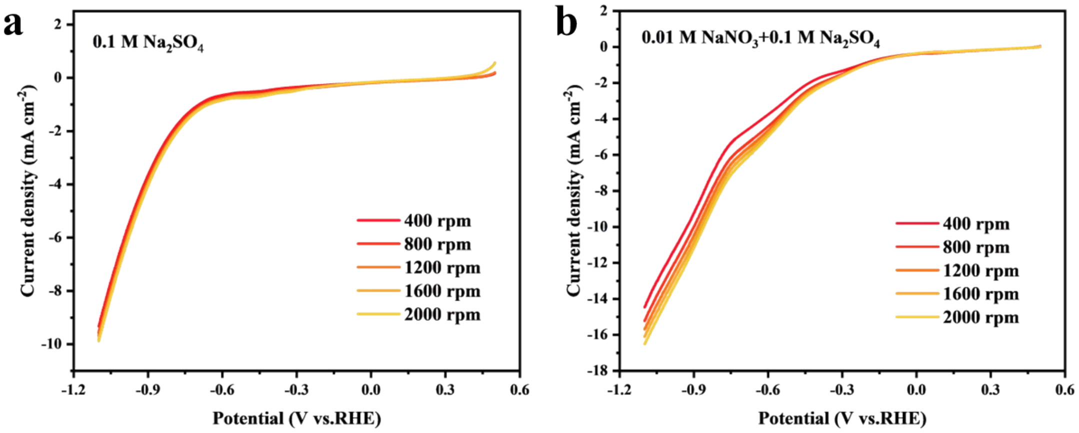

Figure. S20. a and **b** LSV curves of the rotating disk electrode (RDE) loaded with Cu$_5$Fe@NC catalyst at various rotation speeds, measured in both nitrate-containing and nitrate-free systems.

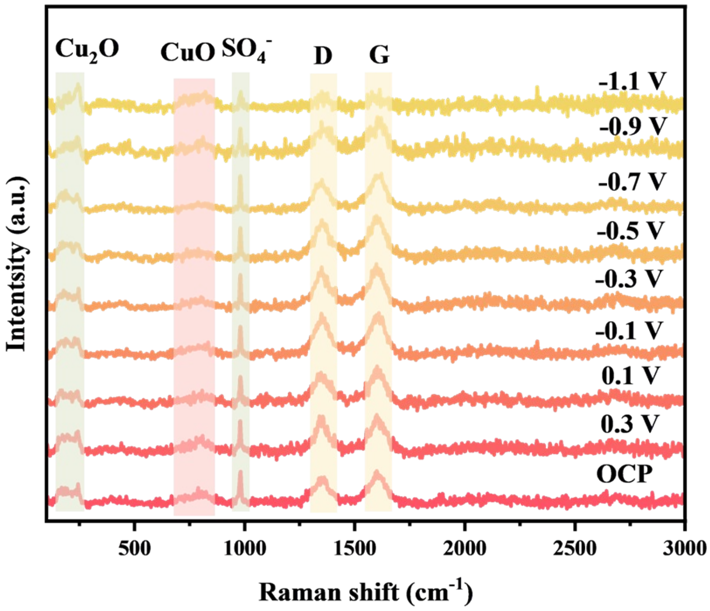

Figure. S21. In-situ Raman spectra of Cu$_5$Fe@NC at various potentials in the absence of nitrate.

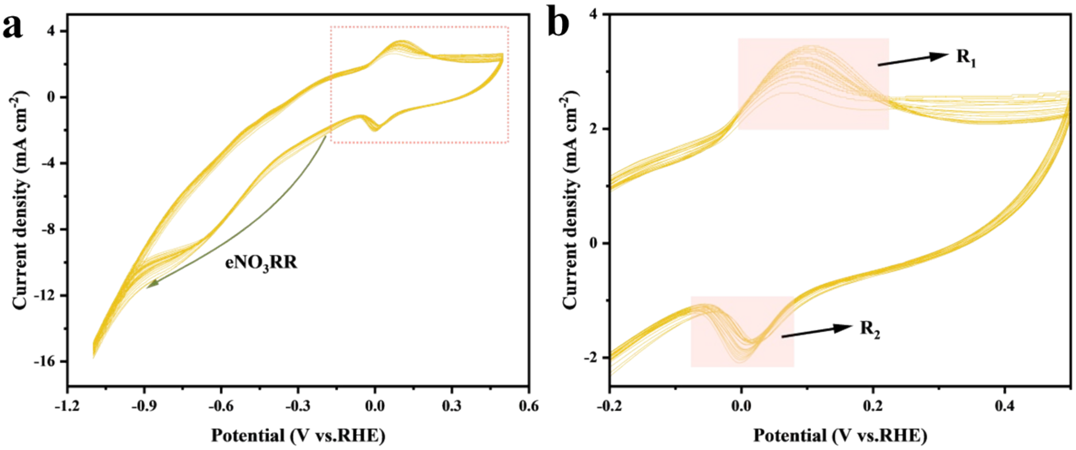

Figure. S22. a and **b** 50-cycle CV curves and the magnified local view of Cu$_5$Fe@NC in a nitrate-containing system, measured at a scan rate of 10 mV s^{-1}.

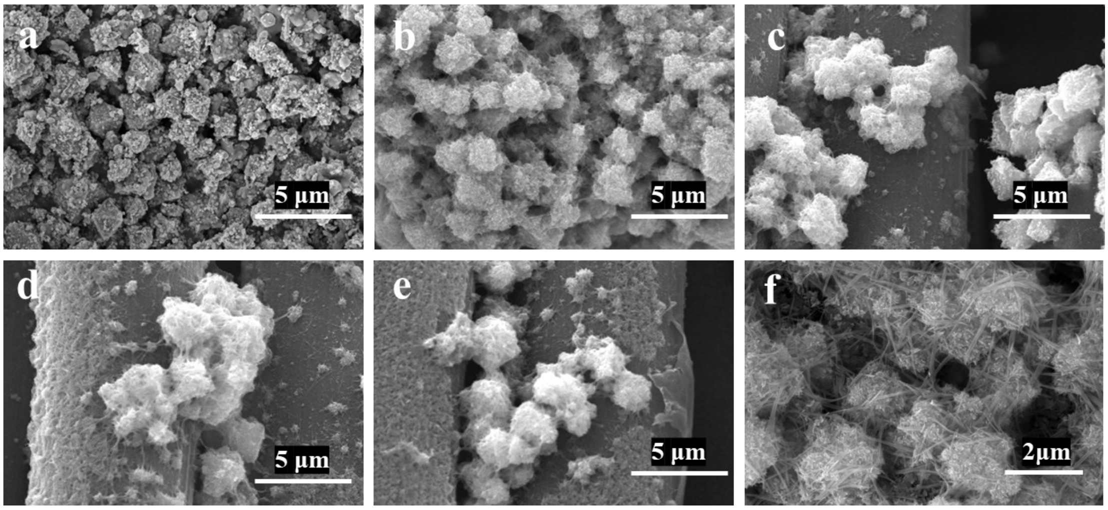

Figure. S23. a SEM image of the Cu_5Fe@NC catalyst before the electrochemical reaction. **(b-f)** SEM images of the Cu_5Fe@NC catalyst after five electrochemical reaction cycles.

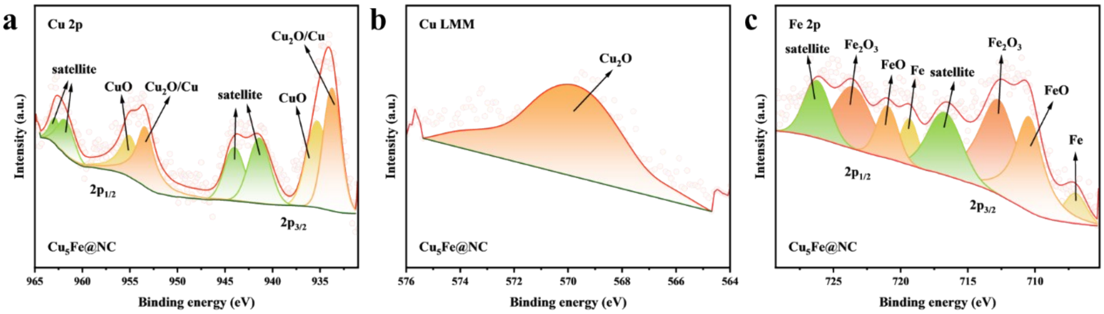

Figure. S24. a, b and c Cu 2p, Cu LMM, and Fe 2p XPS spectra of the Cu_5Fe@NC catalyst after five electrochemical reaction cycles.

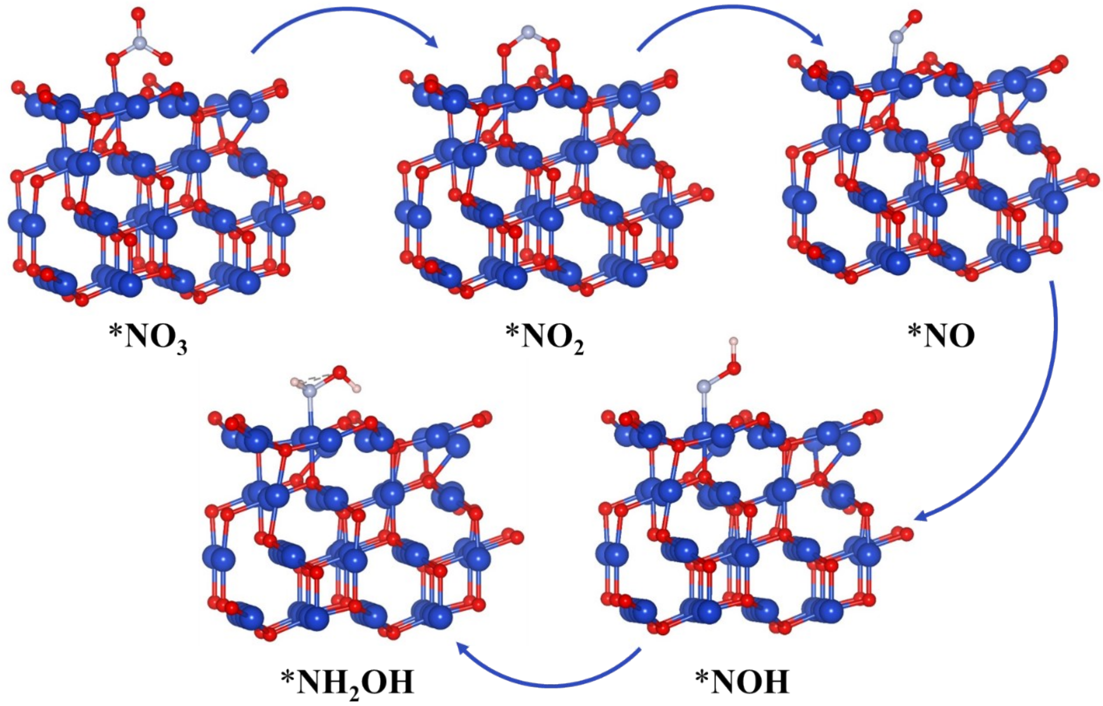

Figure. S25. Structural model diagram illustrating the conversion of NO_3^- to NH_2OH on the Cu_2O surface.

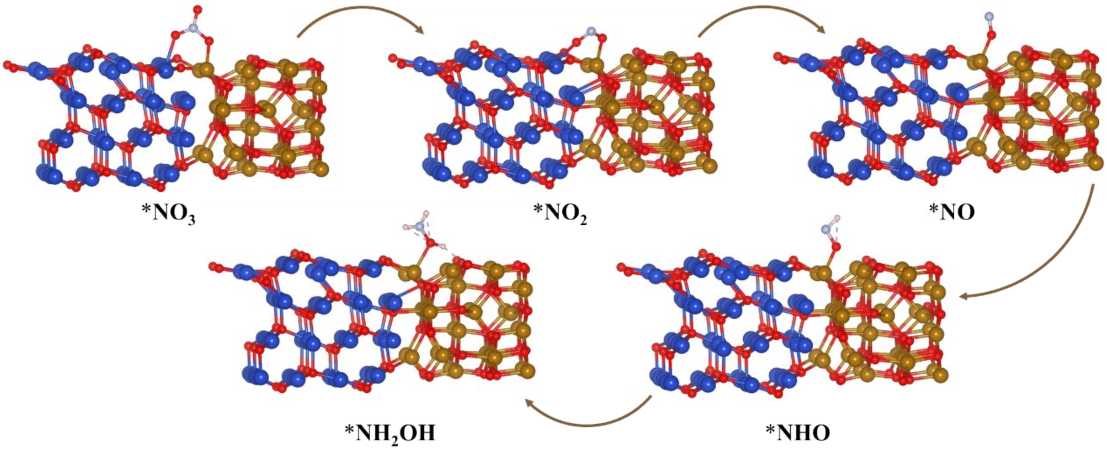

Figure. S26 Structural model diagram depicting the conversion of NO_3^- to NH_2OH at the Cu_2O/Fe_3O_4 heterojunction interface.

3 Supplementary Tables

Table S1: Cu/Fe molar ratios in different $Cu_xFe@NC$ samples as determined by ICP-OES.

Sample name		Cu (mg/L)	Fe (mg/L)	Cu/Fe mole ratio	Average ratio
$Cu_7Fe@NC$	Sample1	69.912	10.273	5.980	5.862
	Sample2	70.121	10.714	5.751	
	Sample3	71.562	10.742	5.854	
$Cu_5Fe@NC$	Sample1	65.737	12.339	4.681	4.658
	Sample2	68.734	12.755	4.735	
	Sample3	72.142	13.904	4.559	
$Cu_3Fe@NC$	Sample1	67.57	21.958	2.704	2.672
	Sample2	61.098	20.351	2.638	
	Sample3	69.574	22.861	2.674	

Table S2: Proportions of surface oxygen chemical bonds and metal oxides in Cu@NC, $Cu_5Fe@NC$, and Fe@NC, determined by XPS peak fitting.

Atomic (%)	Cu@NC	$Cu_5Fe@NC$	Fe@NC
O-Metal	11.11	33.83	43.68
Cu Metal	46.42	0	/
Cu_2O	47.76	78.12	/
CuO	5.82	21.88	/
Fe Metal	/	4.82	16.25
FeO	/	84.64	70.61
Fe_2O_3	/	10.54	13.14

Table S3: Comparison of NH_3 yield and Faradaic efficiency of various reported electrocatalysts for nitrate reduction under similar conditions.

Catalysts	Electrolyte conditions	applied potential (vs. RHE)	NH_3 yield	FE(%)
$Cu_5Fe@NC$ (This work)	0.1M Na_2SO_4+0.01MNaNO_3	−0.7	973.42 μg h^{-1} cm^{-1}	81.58
RuNi-MOFs[5]	0.1MNa_2SO_4+50ppmNO_3^--N	−1.1	274 mg h^{-1} $mg_{cat.}^{-1}$	73
Fe/Ni_2P[6]	0.2MK_2SO_4+50mMNO_3^-	−0.4	4.17mg h^{-1} cm^{-2}	94.3
$La_2Cu_{0.8}Co_{0.2}O_4$[7]	0.5MNa_2SO_4+50ppmNO_3^-	−0.68	69.9μmol h^{-1}·$mg_{cat.}^{-1}$	75
Cu_2O[8]	0.5MNa_2SO_4+200ppmNO_3^-	−0.6	0.0699mmol h^{-1} $mg_{cat.}^{-1}$	85.26
$LF_{0.9}Cu_{0.1}$[9]	0.5MNa_2SO_4+0.01MNaNO_3	−0.9	349 ± 15 μg h^{-1} $mg_{cat.}^{-1}$	48±2

Cl-Cu[10]	50ppm NO_3^--N	−0.65	789 $\mu g\ h^{-1}\ cm^{-2}$	82.5
Cu-Pd/C[11]	0.1MKOH+10mMKNO_3	−0.4	220.8 $\mu g\ mg_{cat.}^{-1}\ h^{-1}$	62.3
Cu(111)[12]	0.1MKOH+10mMKNO_3	−0.5	2.16 $mg\ mg_{cat..}^{-1}\ h^{-1}$	81.1
Ag_2Cu_4[13]	0.5MNa_2SO_4+500ppmNO_3^-	−0.6	0.138 $mmol \cdot h^{-1} \cdot mg_{cat.}^{-1}$	84.6
Ru NCs/TiO_2 NTs[14]	100 ppm NO_3^--N	−0.4	600 $\mu g\ h^{-1}\ cm^{-2}$	>90

Table S4: Surface metal oxide composition of the Cu_5Fe@NC catalyst at different stages, based on XPS peak fitting results.

Proportion	Before activation	After activation	After five cycles
Cu_2O	78.12	54.44	53.77
CuO	21.88	45.56	46.23
Fe Metal	4.82	33.57	8.13
FeO	84.64	27.63	39.84
Fe_2O_3	10.54	38.80	52.03

Table S5: Proportions of surface metal oxides in Cu_5Fe@NC before and after five electrochemical reaction cycles, based on XPS peak fitting results.

Proportion	After activation	After five cycles
Cu_2O/CuO	1.195	1.163
Fe_2O_3/FeO	1.404	1.306

Table S6: Adsorption Gibbs free energies of intermediates during the eNO_3RR process.

Intermediate	Cu_2O	Cu_2O/Fe_3O_4
G(NO_3^-)	0	0
G(*NO_3)	-3.51eV	-4.49 eV
G(*NO_2)	-5.16 eV	-5.98 eV
G(*NO)	-6.06 eV	-7.22 eV
G(*NOH)	-5.87 eV	-8.21 eV
G(*NH_2OH)	-7.00 eV	-9.01 eV

Supplementary References

1 Y. Qu, X. Li, Y. Xia, H. Lan, L. Ding, J. Zhong and X. Chang, *J. Environ. Sci.*, DOI:10.1016/j.jes.2025.03.032.

2 M. Sun, G. Wu, L. Dai, M. Oschatz and Q. Qin, *Catal. Sci. Technol.*, 2022, **12**, 6572–6580.

3 T. Lazaridis, B. M. Stühmeier, H. A. Gasteiger and H. A. El-Sayed, *Nat. Catal.*, 2022, **5**, 363–373.

4 C. Li, Q. Zheng, Q. Xiang, L. Yu, P. Chen, D. Gao, Q. Liu, F. He, D. Yu, Y. Liu and C. Chen, *J. Chem. Educ.*, 2021, **98**, 3026–3031.

5 J. Qin, K. Wu, L. Chen, X. Wang, Q. Zhao, B. Liu and Z. Ye, *J. Mater. Chem. A*, 2022, **10**, 3963–3969.

6 R. Zhang, Y. Guo, S. Zhang, D. Chen, Y. Zhao, Z. Huang, L. Ma, P. Li, Q. Yang, G. Liang and C. Zhi, *Adv. Energy Mater.*, 2022, **12**, 2103872.

7 Z. Gong, W. Zhong, Z. He, C. Jia, D. Zhou, N. Zhang, X. Kang and Y. Chen, *Catal. Today*, 2022, **402**, 259–265.

8 Z. Gong, W. Zhong, Z. He, Q. Liu, H. Chen, D. Zhou, N. Zhang, X. Kang and Y. Chen, *Appl. Catal. B Environ. Energy*, 2022, **305**, 121021.

9 K. Chu, W. Zong, G. Xue, H. Guo, J. Qin, H. Zhu, N. Zhang, Z. Tian, H. Dong, Y.-E. Miao, M. B. J. Roeffaers, J. Hofkens, F. Lai and T. Liu, *J. Am. Chem. Soc.*, 2023, **145**, 21387–21396.

10 B. Zhou, G. Zhan, Y. Yao, W. Zhang, S. Zhao, F. Quan, C. Fang, Y. Shi, Y. Huang, F. Jia and L. Zhang, *Water Res.*, 2023, **242**, 120256.

11 Z. Wang, C. Sun, X. Bai, Z. Wang, X. Yu, X. Tong, Z. Wang, H. Zhang, H. Pang, L. Zhou, W. Wu, Y. Liang, A. Khosla and Z. Zhao, *ACS Appl. Mater. Interfaces*, 2022, **14**, 30969–30978.

12 K. Wu, C. Sun, Z. Wang, Q. Song, X. Bai, X. Yu, Q. Li, Z. Wang, H. Zhang, J. Zhang, X. Tong, Y. Liang, A. Khosla and Z. Zhao, *ACS Mater. Lett.*, 2022, **4**, 650–656.

13 G. Ma, F. Sun, L. Qiao, Q. Shen, L. Wang, Q. Tang and Z. Tang, *Nano Res.*, 2023, **16**, 10867–10872.

14 W. Qiu, M. Xie, P. Wang, T. Gao, R. Li, D. Xiao, Z. Jin and P. Li, *Small*, DOI:10.1002/smll.202300437.